Research Article

Nano Research
2023, 16(2): 2528–2535

ISSN 1998-0124 CN 11-5974/O4
https://doi.org/10.1007/s12274-022-5168-7

Three-dimensional MXene-encapsulated porous Ni-NDC nanosheets as anodes for enhanced lithium-ion batteries

Yuxin Shi[1,§], Guoyin Zhu[2,§], Xiaotian Guo[1], Qingling Jing[1], Huan Pang[1] (✉), and Yizhou Zhang[2] (✉)

[1] *School of Chemistry and Chemical Engineering, Yangzhou University, Yangzhou 225002, China*
[2] *Institute of Advanced Materials and Flexible Electronics (IAMFE), School of Chemistry and Materials Science, Nanjing University of Information Science and Technology (NUIST), Nanjing 210044, China*
[§] *Yuxin Shi and Guoyin Zhu contributed equally to this work.*

Received: 7 September 2022 / **Revised:** 5 October 2022 / **Accepted:** 7 October 2022

ABSTRACT

Although metal–organic frameworks have been heavily tested as the anode materials for lithium-ion batteries (LIBs), the poorer conductivity, easy collapse of frameworks, and serious volume expansion limit their further application in LIBs. Herein, we report a facile approach to obtain MXene-encapsulated porous Ni-naphthalene dicarboxylic acid (Ni-NDC) nanosheets by hybridizing ultrathin Ti_3C_2 MXene and three-dimensional (3D) Ni-NDC nanosheet aggregates. In the structure of Ni-NDC/MXene hybrids, the interlayer hydrogen-bond interaction between Ni-NDC and MXene can effectively increase the interlayer spacing and further inhibit the oxidation of pure MXene. Hence, the introduction of MXene (a conductive matrix) could further improve the conductivity of Ni-NDC, avoid self-agglomeration, and buffer the volume expansion of Ni-NDC nanosheets. Benefiting from the synergistic effects between Ni-NDC and MXene, Ni-NDC/MXene hybrid electrode exhibits a reversible discharge capacity (579.8 $mA{\cdot}h{\cdot}g^{-1}$ at 100 $mA{\cdot}g^{-1}$ after 100 cycles) and good long-term cycling performance (310 $mA{\cdot}h{\cdot}g^{-1}$ at 1 $A{\cdot}g^{-1}$ after 500 cycles).

KEYWORDS

metal–organic framework, MXene, three-dimensional porous intercalation structure, lithium-ion battery

1 Introduction

As a new generation of porous materials with crystal network structure, metal–organic frameworks (MOFs) have been widely applied in numerous research fields (drug delivery [1, 2], sensors [3], gas separation/storage [4], catalysis [5–9], supercapacitors [10–12], batteries [13–15], and other applications [16–18]). Up till now, some kinds of MOFs, owning higher porosity and larger specific surface area, have been tested as electrode materials in lithium-ion batteries (LIBs) [19–21]. On one hand, the inorganic building units in MOFs, such as metal ions or metal oxides, could serve as active sites in the electrochemical process [22, 23]. On the other hand, the porosity of MOFs can provide controllable channels for movement and customized locations for the deposition of the guest molecules [24–27].

However, MOF-based anode materials are still faced with the problems of poor conductivity, easy collapse of frameworks, and serious volume expansion, which may result in poor stability in the repeated charge–discharge processes [28]. Therefore, various reports have been devoted to designing new types of MOF electrode materials with appropriate morphology to achieve rapid diffusion of lithium ions by selecting proper central ions and organic ligands [29, 30]. According to the intercalation–deintercalation mechanism, Li ions are mainly reversibly inserted into the organic components, especially the carboxylic acid group [31–33]. Therefore, 1,4-benzenedicarboxylate and 1,3,5-benzenedicarboxylate, as the most commonly carboxylic acid groups, have been applied to obtain MOF-based electrode materials. In numerous MOFs containing transition metal ions (Ni, Co, Fe, Zn, Cu, etc.) as well as carboxylate groups, Ni-MOF, using 2,6-naphthalene dicarboxylic acid (2,6-NDC) as organic ligand, stands out because of its stable three-dimensional (3D) porous structure, larger specific surface area, excellent electrolyte accessibility, as well as higher diffusion rate of Li^+ [34, 35]. Hence, a novel strategy to obtain the hybrids via introducing functional materials (carbon fibers/tubes, graphene, (reduced) graphene oxide, conductive polymers (PPy), and MXene) into pure MOFs [36], which can retain the excellent characteristics (higher porosity, structural diversity, and larger surface area) of MOFs and physicochemical properties of these functional materials [37, 38]. Therefore, the composite could exhibit excellent conductivity, more stable structure, and enhanced lithium storage performance.

In recent year, MXenes have gathered attention in the field of electrochemical energy storage [39–41], due to the shortened ion-diffusion pathway, higher surface-area-to-volume ratio, as well as faster charge transport [42, 43]. The formula of common MXene is $M_{n+1}X_nT_x$, where M stands for transition metals (V, Zr, Ti, and Ta), X is mainly the element C and/or O, and T_x represents surface terminal groups (–OH, –O, and/or –F) [44, 45]. However, MXene nanosheets are mainly faced with the problems of aggregation, self-stacking, and surface oxidation [46]. To settle the drawbacks of self-accumulation and easy oxidation of MXene, combining MXene with multi-dimensional materials could realize excellent lithium-storage performance [47, 48].

Address correspondence to Huan Pang, huanpangchem@hotmail.com; Yizhou Zhang, zhang@nuist.edu.cn

Due to the good conductivity of MXene as well as the high porosity of MOF, it has been demonstrated that hybridizing MOF with MXene to obtain porous hybrids with enhanced electrochemical performance in LIBs is an effective and convenient method [49]. Herein, we report a simple approach to obtain MXene-encapsulated porous Ni-NDC nanosheets by hybridizing ultrathin Ti_3C_2 MXene and 3D Ni-NDC nanosheet aggregates. In the structure of Ni-NDC/MXene hybrids, the interlayer hydrogen-bond interaction between Ni-NDC and MXene could effectively increase interlayer spacing and further inhibit the oxidation of pure MXene. Hence, the introduction of MXene (a conductive matrix) could further improve the conductivity of Ni-NDC, avoid self-agglomeration, and buffer the volume expansion of Ni-NDC nanosheets. Benefiting from the synergistic effects between Ni-NDC and MXene, Ni-NDC/MXene hybrid electrode exhibits a reversible discharge capacity (579.8 $mA{\cdot}h{\cdot}g^{-1}$ at the current density of 100 $mA{\cdot}g^{-1}$ after 100 cycles) and good long-term cycling performance (310 $mA{\cdot}h{\cdot}g^{-1}$ at the current density 1 $A{\cdot}g^{-1}$ even after 500 cycles). This report can not only overcome the common drawbacks of poorer cycling stability as well as a shorter battery life of Ni-NDC materials, but also provide a facile strategy to prepare low-cost as well as efficient anode materials in LIBs.

2 Results and discussion

The detailed synthesis process of Ni-NDC/MXene hybrids can be seen in Fig. 1. Flower-like Ni-NDC structures, which were self-assembled by ultrathin nanosheets, were firstly obtained by a facile hydrothermal method with nickel nitrate as a nickel source and 2,6-NDC as organic ligand. Hence, the suspension of MXene nanosheets was synthesized by selectively etching the Al layer with a mixed solution of HCl, HF, and LiCl and a series of subsequent operations (centrifugation and ultrasonic dispersion) in Fig. S1 in the Electronic Supplementary Materials (ESM). Then, the resulting MXene suspension was added dropwise into the aqueous solution of Ni-NDC particles, which were modified by poly(diallyldimethylammonium chloride) (PDDA). As shown in Fig. S2 in the ESM, electrostatic adsorption between Ni-NDC and MXene is obvious and many grey particles appear at the bottom of the beaker, which exhibit the successful combination of Ni-NDC and MXene. At last, 3D MXene-encapsulated porous Ni-NDC nanosheets were successfully obtained through normal temperature stirring, centrifugation, and calcination under low temperatures.

The scanning electron microscopy (SEM) images under different magnifications of Ni-NDC (Figs. 2(a) and 2(b)) reveal that each 3D flower-like Ni-NDC structure is composed of various single small-size nanosheets owning uniform thickness. As shown in Fig. S3 in the ESM, the thickness decreased with the increase in synthesis temperature. When the reaction temperature is too high or too low, the size of the nanosheets becomes uneven and the degree of self-assembly is poor, resulting in the problem of self-accumulation. Moreover, the transmission electron microscopy (TEM) image of Ni-NDC (Fig. 2(c)) exhibits that the obtained Ni-NDC nanosheets are almost transparent, representing ultrathin nanostructures. To further increase the specific surface and preserve porosity, the low-temperature calcination method was applied to further activation of Ni-NDC, which can remove the guest solvent molecules in MOFs and transform from ordered MOFs into disordered MOFs to enhance the lithium storage performance of MOFs. The SEM images of Ni-NDC nanosheets obtained at different calcination temperatures can be seen in Fig. S4 in the ESM. As shown in Fig. 2(d), MXene shows ultrathin and almost transparent single-layer flakes, which also has good crystallinity. The detailed morphological structures of Ni-NDC/MXene hybrids with different mass ratios of MXene and Ni-NDC (Figs. 2(e)–2(l)) show that ultrathin Ni-NDC nanosheets are well-distributed in the MXene framework. Both high-resolution TEM (HRTEM) images (Figs. 2(m)–2(o)) and selected area electron diffraction (SAED) pattern (Fig. 2(p)) prove the excellent crystallinity of MXene nanosheets and the successful combination of Ni-NDC and MXene. More specifically, the lattice spacing of fringes is 0.17 nm, which represents the (100) plane of MXene. High-angle annular dark-field scanning TEM (HAADF-STEM) and energy dispersive spectroscopy (EDS) mapping images exhibit that the elements (Ni, C, O, and Ti) are well-distributed in Ni-NDC/MXene hybrids (Fig. 2(q)). In summary, the above results confirm that MXene-encapsulated porous Ni-NDC nanosheets are successfully obtained in this work.

As shown in Fig. 3(a), all the obtained samples (MXene, Ni-NDC, and Ni-NDC/MXene-2) exhibit good crystallinity, with sharp and intense peaks in X-ray diffraction (XRD) patterns. Firstly, the main peaks of Ni-NDC are located at 7.0°, 14.18°, and 14.82°. After introducing MXene, a new characteristic peak, which corresponds to the (002) diffraction peak of MXene, appeared in the Ni-NDC/MXene-2, confirming the successful synthesis of Ni-NDC/MXene hybrids. However, the (002) peak in Ni-NDC/MXene hybrids moved to a lower angle of 6.2° in comparison with that of MXene. The further increased interlayer spacing strongly indicates that MXene-encapsulated porous Ni-NDC nanosheets could effectively overcome the self-accumulation of Ni-NDC or MXene nanosheets, thus providing convenience for Li^+ during electrochemical reaction and ensuring high-rate capability. Hence, the intensity of the peaks located at 14.18° and 14.82° increases, because the introduction of MXene can further influence the growth direction of the Ni-NDC crystals. Similarly, Raman spectra of MXene, Ni-NDC, and Ni-NDC/MXene-2 can be seen in Fig. 3(b), which confirm that Ni-NDC and MXene have successfully compounded. Analyzing from Figs. 3(c) and 3(d), the *R* space height and corresponding coordination number of Ni-NDC slightly decreased with the introduction of MXene.

The main elements in Ni-NDC are C, O, and Ni (Fig. S5 in the ESM), while MXene contains the elements of Ti, C, and O. Firstly, Fig. S6 in the ESM exhibits X-ray photoelectron spectroscopy (XPS) full spectrum of Ni-NDC/MXene, where the signals of Ni

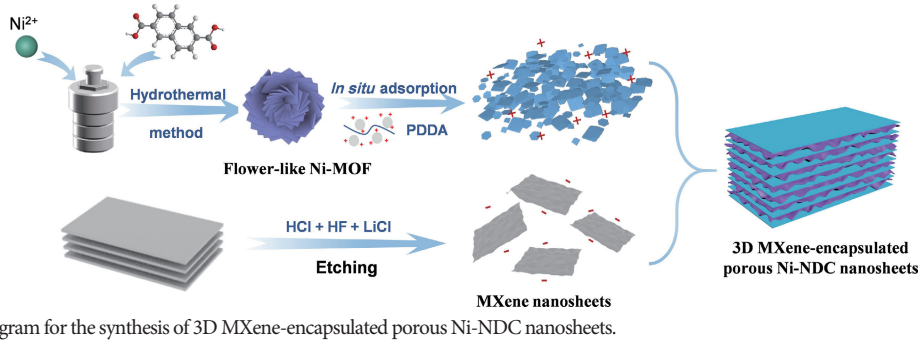

Figure 1 Schematic diagram for the synthesis of 3D MXene-encapsulated porous Ni-NDC nanosheets.

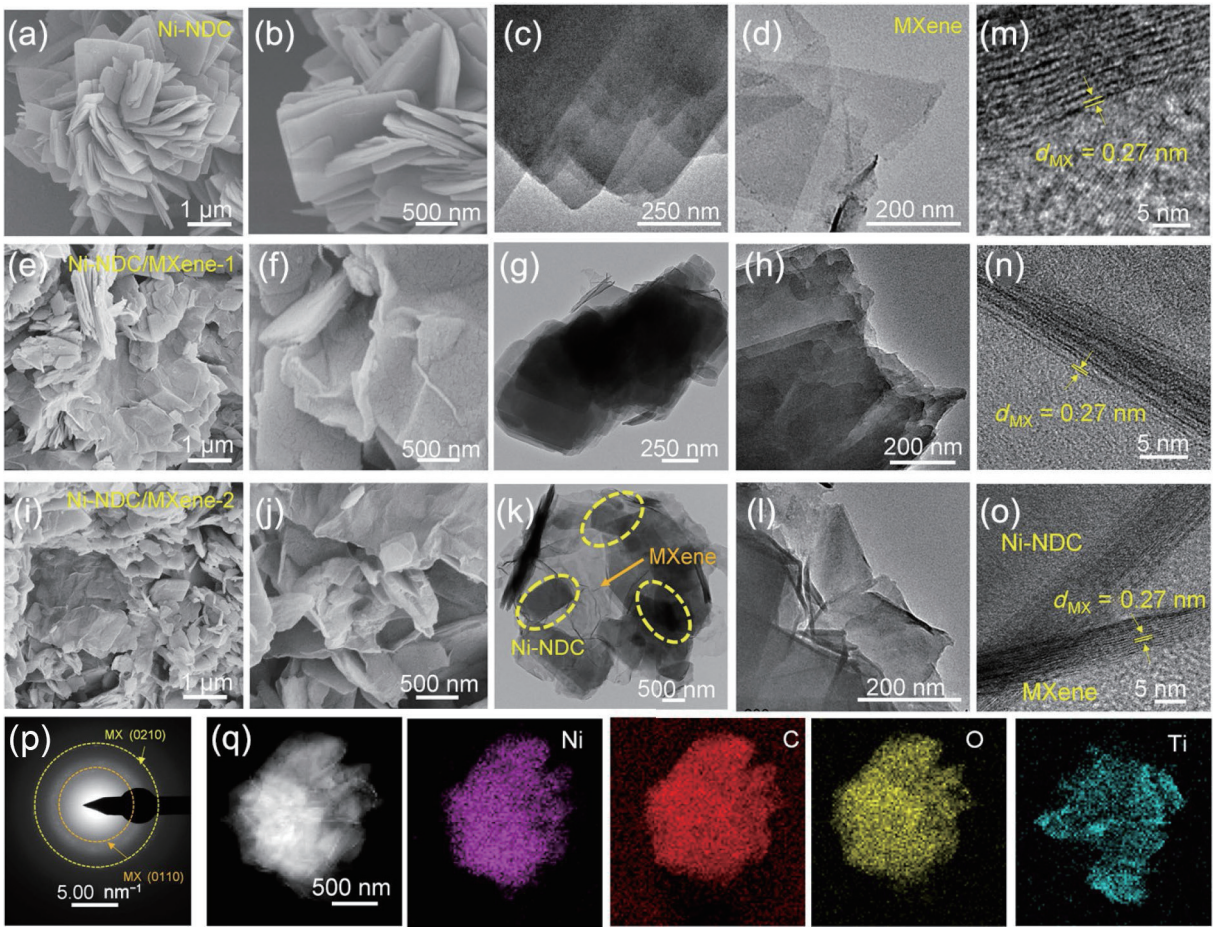

Figure 2 SEM images: (a) and (b) Ni-NDC, (e) and (f) Ni-NDC/MXene-1, and (i) and (j) Ni-DC/MXene-2. TEM images: (c) Ni-NDC, (d) Mxene, (g) and (h) Ni-NDC/MXene-1, and (k) and (l) Ni-NDC/MXene-2. HRTEM images: (m) Mxene, (n) Ni-NDC/MXene-1, (o) Ni-NDC/MXene-2. (p) SAED pattern of Ni-NDC/MXene-2. (q) EDS elemental mapping images of Ni-NDC/MXene-2.

2p, Ti 2p, O 1s, and C 1s are located at 855, 459, 532, and 288 eV, which confirms that Ni-NDC/MXene hybrids are composed of MXene and Ni-NDC [50, 51]. The Ti 2p spectra of the MXene can be seen in Fig. 3(e), which are resolved into six peaks [52]. Hence, the peak for TiO_2 can not been seen in the Ti 2p spectra of Ni-NDC/MXene, which indicates that the strong hydrogen bonding between MXene and Ni-NDC can slow down the oxidation rate and further enhance the stability of MXene. Figure 3(f) exhibits that the Ni 2p spectra in Ni-NDC/MXene hybrids transfer to lower binding energies in comparison with those in Ni-NDC (Fig. S7 in the ESM), which can be attributed to the connection between the organic ligand (2,6-NDC) in Ni-NDC and surface functional groups (–F, –OH, etc.) from MXene. All XPS spectra exhibit two peaks corresponding to Ni $2p_{3/2}$ as well as Ni $2p_{1/2}$, which are determined by the spin-orbit characteristics of nickel ions. As can be seen in Fig. S8 in the ESM, the peaks for Ni-NDC are located at 284.3, 285.1, 287.8, and 288.4 eV, which represent the valence bonds, including C=C, C–C, C=O, and O=C–O, respectively. Additionally, the C 1s spectra of Ni-NDC/MXene exhibit another peak corresponding to C–Ti located at 280.7 eV, which indicate that MXene exists in the obtained composites. Analyzing from Fig. S9 in the ESM, the thermal stability of Ni-NDC nanosheets has been successfully enhanced with the introduction of MXene. The chemical structure of the obtained Ni-NDC has been further tested by Fourier transform infrared spectroscopy (FTIR) in Fig. S10 in the ESM. In Fig. S11 in the ESM, the Brunauer–Emmett–Teller (BET) surface of Ni-NDC/MXene-2 is 87.753 $m^2 \cdot g^{-1}$, much higher than that of pure MXene (25.232 $m^2 \cdot g^{-1}$) and Ni-NDC (55.672 $m^2 \cdot g^{-1}$).

Analyzing the cyclic voltammetry (CV) of Ni-NDC/MXene-2 (Fig. 4(a)), two peaks are easily observed in the first turn of the CV curve. More detailly, the first peak (~ 1.12 V) could be attributed to the formation of the solid–electrolyte interface (SEI) layer as well as the irreversible lithium process of C-O, while another peak (~ 7.0 V) corresponds to the reaction of lithium ion with C-C aromatic rings and trapping of Li^+ between MXene and Ni-NDC [53]. Hence, the CV curves of Ni-NDC, MXene, and Ni-NDC/MXene-1 anode materials can be seen in Figs. S12, S13(c), and S14 in the ESM, respectively. According to the reported work, lithium ion is mostly reversible intercalation/delamination from organic parts (consisting of benzene rings as well as carboxyl groups [54]) without the direct participation of nickel ions [55, 56]. What's more, the third cycle in the CV curve is similar to that of the second cycle, confirming that the Ni-NDC/MXene anode shows the advantages of high reversibility and stability in the electrochemical reaction process.

As shown in Fig. S15 in the ESM, the Ni-NDC nanosheets obtained at the calcination temperature of 150 °C exhibit an enhanced cycling performance, in comparison with other two samples. Although pure Ni-NDC anode exhibits an excellent initial capacity (2,139.5 $mA \cdot g^{-1}$), the specific discharge capacity decreases quickly in the first 20 cycles and only remains about 99 $mA \cdot g^{-1}$ in Fig. 4(b). The higher initial capacity is because the porosity of Ni-NDC provides a channel for the transmission of Li^+ as well as electrons, while the pure Ni-NDC shows poor cycling performance as a result from the unstable framework and poor conductivity. Figures S13(a) and S13(b) in the ESM display the cycling performance of MXene under different current densities, which demonstrate that the initial discharge capacity of MXene is poor. Hence, Fig. S16 in the ESM shows the charge–discharge

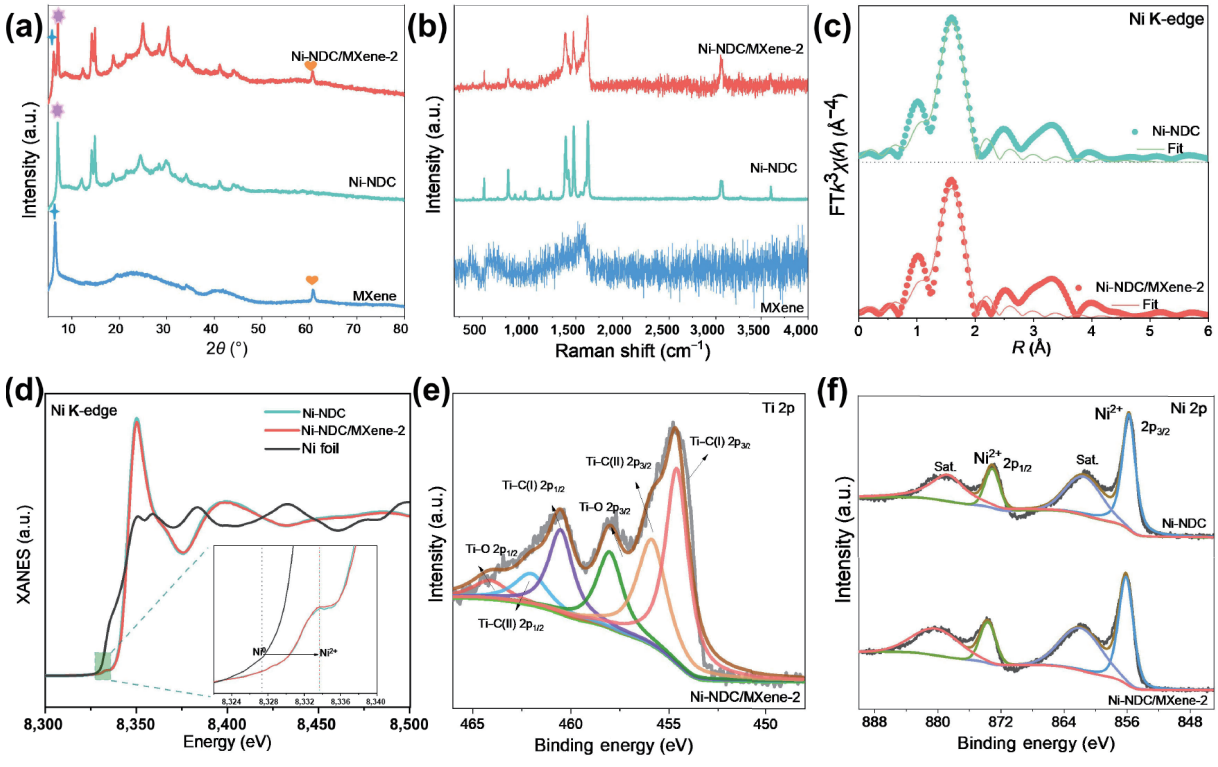

Figure 3 (a) XRD patterns of MXene, Ni-NDC, and Ni-NDC/MXene-2. (b) Raman spectra of MXene, Ni-NDC, and Ni-NDC/MXene-2. (c) *R* spaces of Ni-NDC and Ni-NDC/MXene-2. (d) Normalized XANES spectra of Ni-NDC and Ni-NDC/MXene-2 at the Ni K-edge with a Ni foil as the reference. (e) Ti 2p spectra and (f) Ni 2p spectra of MXene, Ni-NDC, and Ni-NDC/MXene-2.

profiles of Ni-NDC, Ni-NDC/MXene-1, and Ni-NDC/MXene-2 for the 1st, 2nd, 3rd, 5th, and 10th cycles at 500 mA·h·g^{-1}. The initial discharge capacity of pure Ni-NDC nanosheets is high. However, the discharge capacity in second cycle is obviously reduced to 35% of the initial discharge capacity, which confirms that Ni-NDC is also faced with the common problem of poor cycle stability. Furthermore, the cycle stability of Ni-NDC/MXene anodes is enhanced with the introduction of MXene, which can keep stable after the second lap without the loss of capacity. More importantly, the groups (–F and –O) from MXene could be bonded to H in –COOH from the organic ligand of Ni-NDC to construct 3D porous Ni-NDC/MXene composites, with the addition of MXene. Therefore, the specific capacities of Ni-NDC/MXene composites improved observably compared with pure Ni-NDC, particularly the specific capacity of Ni-NDC/MXene-2 could still maintain 579.8 mA·h·g^{-1} at the current density of 500 mA·g^{-1} even after 100 cycles in Fig. 4(b). What's more, even under a lower current density of 200 mA·g^{-1} (Fig. S17 in the ESM), Ni-NDC/MXene-2 also exhibits an enhanced cycling stability. As expected, the Ni-NDC/MXene-2 also exhibits excellent long-term cycling stability in Fig. 4(d). The obtained electrode shows a specific discharge/charge capacity (~ 2,081.6/1,002.8 mA·h·g^{-1}) in the first cycle, with a corresponding Coulombic efficiency of 48% and almost 100% afterwards. Even after 500 cycles, the Ni-NDC/MXene-2 electrode achieves an excellent discharge capacity of 310 mA·h·g^{-1} at the current density of 1 A·g^{-1}. Hence, the rate capacity of Ni-NDC/MXene-2 composite is much better than those of pure Ni-NDC and Ni-NDC/MXene-1 (Fig. 4(c)). More detailly, the discharge capacity of Ni-NDC/MXene-2 only decreases from 717.7 to 369.3 mA·h·g^{-1}, as the current density increases from 0.1 to 1.0 A·g^{-1}. Figure S18 in the ESM shows the Nyquist plots of Ni-NDC, Ni-NDC/MXene-1, and Ni-NDC/MXene-2 before and after cycling. The Ni-NDC/MXene-2 anode has the smallest semicircle diameter in the high-medium frequency region. Thus, it exhibits higher charge-transfer kinetics and excellent electrical conductivity. To further intuitively reflect the lithium-storage performance of the obtained Ni-NDC/MXene anode, we have compared the discharge capacities of other MOFs as anode materials for LIBs in previous work (Fig. 4(e)) [57–65].

The above results confirm that Ni-NDC/MXene shows enhanced lithium storage in terms of superior cycling performance as well as enhanced capacity due to 3D porous frameworks and coupling effect between MXene and Ni-NDC. Moreover, the 3D porous frameworks can further settle the drawbacks of self-accumulation as well as volume expansion of Ni-NDC and MXene in the process of electrochemical reaction. As the mass of MXene increases, the interlayer spacing and specific surface area of the Ni-NDC/MXene hybrids also increase, which undoubtedly accelerate the diffusion and transmission of lithium ions.

For further investing the kinetic properties and lithium-ion mechanism of the Ni-NDC/MXene hybrids, the CV measurements of Ni-NDC, Ni-NDC/MXene-1, and Ni-NDC/MXene-2 electrodes were conducted with the scan rate recorded from 0.2 to 1.0 mV·s^{-1} (Fig. 5(a) and Figs. S19 and S20 in the ESM). The relation between peak current and sweep rate is indicated by Eq. (1) [66]

$$\log(i) = a + b\log(v) \quad (1)$$

In Eq. (1), i represents peak current, v is scan rate, and a and b are adjustable parameters. For the diffusion- or capacitive-controlled process, the values of b are equal to 0.5 and 1.0, respectively. When the value of b is between 0.5 and 1.0, the mixed mechanism can be found [12, 67]. As can be seen in Fig. 5(b), the slope values in the linear curves are 0.623 and 0.644, indicating that both pseudocapacitive- and diffusion-controlled reaction processes could be found in the lithium storage mechanism. The contribution of capacitance and diffusion of Ni-NDC/MXene-2 samples to current is calculated by Eq. (2)

$$i = k_1 v + k_2 v^{1/2} \quad (2)$$

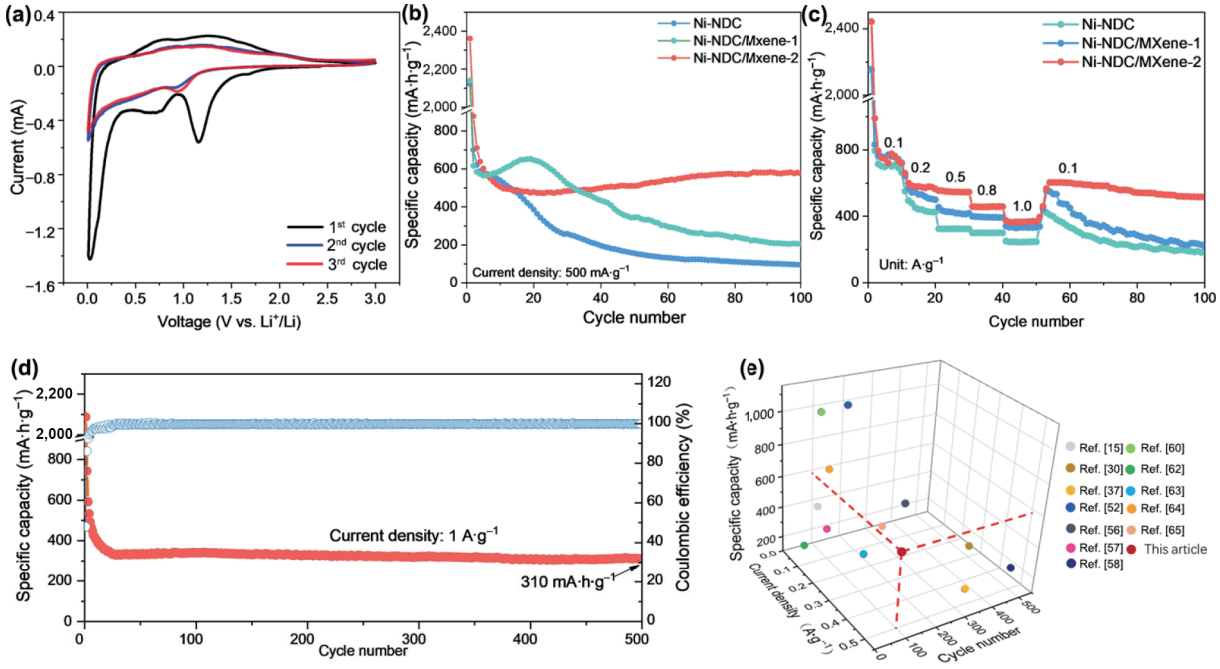

Figure 4 (a) CV curves of Ni-NDC/MXene-2 in the range of 0.001–3.0 V (vs. Li/Li^+) and scan rate at 0.1 $mV·s^{-1}$. (b) Cycle performance and (c) rate capacities of Ni-NDC, Ni-NDC/MXene-1, and Ni-NDC/MXene-2. (d) Long-cycle performance of Ni-NDC/MXene-2. (e) Comparison of the cycling performance in this work with the recently reported MOF-based anode materials, which is obtained from Table S1 in the ESM.

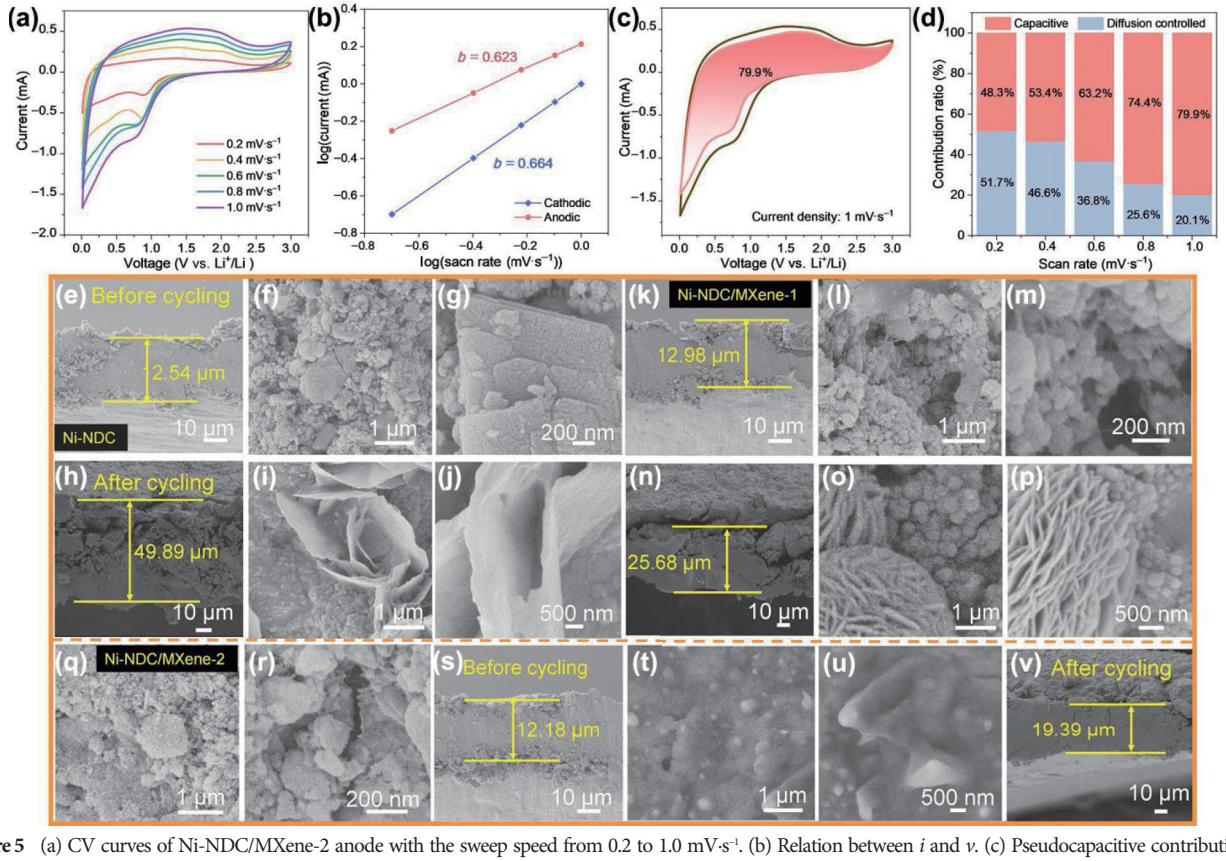

Figure 5 (a) CV curves of Ni-NDC/MXene-2 anode with the sweep speed from 0.2 to 1.0 $mV·s^{-1}$. (b) Relation between *i* and *v*. (c) Pseudocapacitive contribution of Ni-NDC/MXene-2 anode at the sweep speed at $mV·s^{-1}$. (d) Percentages of capacitive and diffusion contributions of Ni-NDC/MXene-2 sample at different scanning rates. The top-view and corresponding cross-sectional SEM images of (e)–(g) pure Ni-NDC before cycling, (h)–(j) pure Ni-NDC after 100 cycles, (k)–(m) Ni-NDC/MXene-1 before cycling, (n)–(p) Ni-NDC/MXene-1 after 100 cycles, (q)–(s) Ni-NDC/MXene-2 before cycling, and (t)–(v) Ni-NDC/MXene-2 after 100 cycles.

where k_1v represents capacitance, $k_2v^{1/2}$ represents diffusion, and k_1 and k_2 are constants.

The percentage of pseudocapacitive-controlled contribution increased from 48.3% to 79.9%, when the current density transforms from 0.2 to 1.0 $mV·s^{-1}$, and the current of the Ni-NDC/MXene-2 anode is largely dominated by the diffusion-controlled capacity (Figs. 5(c) and 5(d)). The enhancement of pseudo-capacitance could be ascribed to abundant mesoporous channels, the higher specific surface area of Ni-NDC, and high conductivity of MXene. Moreover, the mixed capacitance mechanism plays a key role in improving the electrochemical performance of Ni-NDC/MXene hybrids.

Furthermore, to determine the cycling stability of Ni-NDC/MXene anode, cross-sectional and surface SEM images of Ni-NDC, Ni-NDC/MXene-1, and Ni-NDC/MXene-2 anodes before and after the cycling test are prepared. Firstly, the pure Ni-NDC anode exhibits a large increase in thickness from 12.34 to 49.89 μm and the structure is destroyed along with the occurrence of side reaction (Figs. 5(e)–5(j)). Analyzing from Figs. 5(k)–5(p), the Ni-NDC/MXene-1 anode exhibits increased thickness from 12.98 to 25.68 μm after 100 cycles, which indicates that the introduction of MXene could effectively decrease the volume expansion and further improve the cycling stability of pure Ni-NDC. However, the Ni-NDC/MXene-1 anode is still faced with the problem of the occurrence of side reactions. More surprisingly, the Ni-NDC/MXene-2 has a slight thickness increase from 12.18 to 19.39 μm, owning a smaller volume expansion and well-preserved structure in Figs. 5(q)–5(v). The enhanced electrochemical properties in LIBs of the Ni-NDC/MXene composites are summarized as follows. On one hand, the introduction of MXene can reduce the volume variation and generate a stable SEI layer, which can further prevent material pulverization and the occurrence of side reactions during charge–discharge processes. On the other hand, encapsulating porous Ni-NDC nanosheets with MXene can further reduce the self-aggregation and improve the conductivity of pure Ni-NDC nanoplates, lower the resistance, and increase the movement rate of lithium ions and electrons.

3 Conclusions

In summary, the 3D MXene-encapsulated porous Ni-NDC nanosheets were successfully obtained and used as the anode materials in LIBs with enhanced rate capability as well as long-term cycling properties. The Ni-NDC/MXene anode exhibited a superior specific capacity (579.8 $mA{\cdot}h{\cdot}g^{-1}$ at the current density of 100 $mA{\cdot}g^{-1}$ after 100 cycles) and maintained 310 $mA{\cdot}h{\cdot}g^{-1}$ at the current of 1 $A{\cdot}g^{-1}$ after 500 cycles with nearly 100% capacity retention, which is much better than the previous reported MXene and MOF-based anode materials. The significant enhancement of lithium storage performance can be ascribed to the 3D porous interpenetrating frameworks and coupling effect between Ni-NDC and MXene, including: (1) The porosity of MOF material provides a controllable channel for the transmission of lithium ions and electrons. Hence, MXene can further enhance the conductivity as well as stability of pure Ni-NDC sample. (2) 3D porous interpenetrating frameworks can overcome the drawbacks of self-accumulation as well as volume expansion of Ni-NDC and MXene in the electrochemical reaction process. (3) With the increase of the mass of MXene, the specific surface area as well as interlayer spacing of the Ni-NDC/MXene hybrids also increased, which undoubtedly accelerate the diffusion and transmission of lithium ion and further enhance the long-term cycling performance and rate capability.

Acknowledgements

This work was supported by the National Natural Science Foundation of China (Nos. 62174085 and 21805136), the Program for Young Changjiang Scholars of the Ministry of Education, the Jiangsu Specially-Appointed Professors Program, the Top-notch Academic Programs Project of Jiangsu Higher Education Institutions (TAPP), the Natural Science Foundation of Jiangsu Province (No. BK20200044), and the Startup Foundation for Introducing Talent of NUIST (No. 2021r091).

Electronic Supplementary Material: Supplementary material (electrochemical measurements, XRD, XPS, and thermogravimetry analysis (TGA)) is available in the online version of this article at https://doi.org/10.1007/s12274-022-5168-7.

References

[1] Cai, W.; Wang, J. Q.; Chu, C. C.; Chen, W.; Wu, C. S.; Liu, G. Metal–organic framework-based stimuli-responsive systems for drug delivery. *Adv. Sci.* **2019**, *6*, 1801526.

[2] Peng, S.; Bie, B. B.; Sun, Y. Z. S.; Liu, M.; Cong, H. J.; Zhou, W. T.; Xia, Y. C.; Tang, H.; Deng, H. X.; Zhou, X. Metal–organic frameworks for precise inclusion of single-stranded DNA and transfection in immune cells. *Nat. Commun.* **2018**, *9*, 1293.

[3] Li, Y.; Ling, W.; Liu, X. Y.; Shang, X.; Zhou, P.; Chen, Z. R.; Xu, H.; Huang, X. Metal–organic frameworks as functional materials for implantable flexible biochemical sensors. *Nano Res.* **2021**, *14*, 2981–3009.

[4] Pei, J. Y.; Wen, H. M.; Gu, X. F.; Qian, Q. S.; Yang, Y.; Cui, Y. J.; Li, B.; Chen, B. L.; Qian, G. D. Dense packing of acetylene in a stable and low-cost metal–organic framework for efficient C_2H_2/CO_2 separation. *Angew. Chem., Int. Ed.* **2021**, *60*, 25068–25074.

[5] Zhuang, Z. C.; Huang, J. Z.; Li, Y.; Zhou, L.; Mai, L. Q. The holy grail in platinum-free electrocatalytic hydrogen evolution: Molybdenum-based catalysts and recent advances. *ChemElectroChem* **2019**, *6*, 3570–3589.

[6] Zhuang, Z. C.; Li, Y.; Huang, J. Z.; Li, Z. L.; Zhao, K. N.; Zhao, Y. L.; Xu, L.; Zhou, L.; Moskaleva, L. V.; Mai, L. Q. Sisyphus effects in hydrogen electrochemistry on metal silicides enabled by silicene subunit edge. *Sci. Bull.* **2019**, *64*, 617–624.

[7] Zhu, P.; Xiong, X.; Wang, D. S. Regulations of active moiety in single atom catalysts for electrochemical hydrogen evolution reaction. *Nano Res.* **2022**, *15*, 5792–5815.

[8] Chen, Y. J.; Gao, R.; Ji, S. F.; Li, H. J.; Tang, K.; Jiang, P.; Hu, H. B.; Zhang, Z. D.; Hao, H. G.; Qu, Q. Y. et al. Atomic-level modulation of electronic density at cobalt single-atom sites derived from metal–organic frameworks: Enhanced oxygen reduction performance. *Angew. Chem., Int. Ed.* **2021**, *60*, 3212–3221.

[9] Zhang, H.; Li, H. Y.; Akram, B.; Wang, X. Fabrication of NiFe layered double hydroxide with well-defined laminar superstructure as highly efficient oxygen evolution electrocatalysts. *Nano Res.* **2019**, *12*, 1327–1331.

[10] Zheng, S. S.; Zhou, H. J.; Xue, H. G.; Braunstein, P.; Pang, H. Pillared-layer Ni-MOF nanosheets anchored on Ti_3C_2 MXene for enhanced electrochemical energy storage. *J. Colloid Interface Sci.* **2022**, *614*, 130–137.

[11] Liu, C. L.; Bai, Y.; Li, W. T.; Yang, F. Y.; Zhang, G. X.; Pang, H. *In situ* growth of three-dimensional MXene/metal–organic framework composites for high-performance supercapacitors. *Angew. Chem., Int. Ed.* **2022**, *61*, e202116282.

[12] Zhang, G. H.; Hu, J.; Nie, Y.; Zhao, Y. L.; Wang, L.; Li, Y. Z.; Liu, H. Z.; Tang, L. Z.; Zhang, X. N.; Li, D. et al. Integrating flexible ultralight 3D Ni micromesh current collector with NiCo bimetallic hydroxide for smart hybrid supercapacitors. *Adv. Funct. Mater.* **2021**, *31*, 2100290.

[13] Zhuang, Z. C.; Li, Y. H.; Yu, R. H.; Xia, L. X.; Yang, J. R.; Lang, Z. Q.; Zhu, J. X.; Huang, J. Z.; Wang, J. O.; Wang, Y. et al. Reversely trapping atoms from a perovskite surface for high-performance and durable fuel cell cathodes. *Nat. Catal.* **2022**, *5*, 300–310.

[14] Ma, L. B.; Lv, Y. H.; Wu, J. X.; Xia, C.; Kang, Q.; Zhang, Y. Z.; Liang, H. F.; Jin, Z. Recent advances in anode materials for potassium-ion batteries: A review. *Nano Res.* **2021**, *14*, 4442–4470.

[15] Wang, Y.; Qu, Q. T.; Liu, G.; Battaglia, V. S.; Zheng, H. H. Aluminum fumarate-based metal–organic frameworks with tremella-like structure as ultrafast and stable anode for lithium-ion batteries. *Nano Energy* **2017**, *39*, 200–210.

[16] Chen, S. H.; Li, W. H.; Jiang, W. J.; Yang, J. R.; Zhu, J. X.; Wang, L. Q.; Ou, H. H.; Zhuang, Z. C.; Chen, M. Z.; Sun, X. H. et al. MOF encapsulating N-heterocyclic carbene-ligated copper single-atom site catalyst towards efficient methane electrosynthesis. *Angew. Chem., Int. Ed.* **2022**, *61*, e202114450.

[17] Liu, Y. W.; Wang, B. X.; Fu, Q.; Liu, W.; Wang, Y.; Gu, L.; Wang,

D. S.; Li, Y. D. Polyoxometalate-based metal–organic framework as molecular sieve for highly selective semi-hydrogenation of acetylene on isolated single Pd atom sites. *Angew. Chem., Int. Ed.* **2021**, *60*, 22522–22528.

[18] Zhang, E. H.; Tao, L.; An, J. K.; Zhang, J. W.; Meng, L. Z.; Zheng, X. B.; Wang, Y.; Li, N.; Du, S. X.; Zhang, J. T. et al. Engineering the local atomic environments of indium single-atom catalysts for efficient electrochemical production of hydrogen peroxide. *Angew. Chem., Int. Ed.* **2022**, *61*, e202117347.

[19] Zhou, D.; Ni, J. F.; Li, L. Self-supported multicomponent CPO-27 MOF nanoarrays as high-performance anode for lithium storage. *Nano Energy* **2019**, *57*, 711–717.

[20] Gao, C. W.; Jiang, Z. J.; Wang, P. X.; Jensen, L. R.; Zhang, Y. F.; Yue, Y. Z. Optimized assembling of MOF/SnO_2/graphene leads to superior anode for lithium ion batteries. *Nano Energy* **2020**, *74*, 104868.

[21] Gao, C. W.; Jiang, Z. J.; Qi, S. B.; Wang, P. X.; Jensen, L. R.; Johansen, M.; Christensen, C. K.; Zhang, Y. F.; Ravnsbaek, D. B.; Yue, Y. Z. Metal–organic framework glass anode with an exceptional cycling-induced capacity enhancement for lithium-ion batteries. *Adv. Mater.* **2022**, *34*, 2110048.

[22] Zheng, S. S.; Li, X. R.; Yan, B. Y.; Hu, Q.; Xu, Y. X.; Xiao, X.; Xue, H. G.; Pang, H. Transition-metal (Fe, Co, Ni) based metal–organic frameworks for electrochemical energy storage. *Adv. Energy Mater.* **2017**, *7*, 1602733.

[23] Kong, L. J.; Liu, M.; Huang, H.; Xu, Y. H.; Bu, X. H. Metal/Covalent–organic framework based cathodes for metal-ion batteries. *Adv. Energy Mater.* **2022**, *12*, 2100172.

[24] Hao, J. C.; Zhuang, Z. C.; Cao, K. C.; Gao, G. H.; Wang, C.; Lai, F. L.; Lu, S. L.; Ma, P. M.; Dong, W. F.; Liu, T. X. et al. Unraveling the electronegativity-dominated intermediate adsorption on high-entropy alloy electrocatalysts. *Nat. Commun.* **2022**, *13*, 2662.

[25] Zheng, X. B.; Li, B. B.; Wang, Q. S.; Wang, D. S.; Li, Y. D. Emerging low-nuclearity supported metal catalysts with atomic level precision for efficient heterogeneous catalysis. *Nano Res.* **2022**, *15*, 7806–7839.

[26] Cui, T. T.; Wang, Y. P.; Ye, T.; Wu, J.; Chen, Z. Q.; Li, J.; Lei, Y. P.; Wang, D. S.; Li, Y. D. Engineering dual single-atom sites on 2D ultrathin N-doped carbon nanosheets attaining ultra-low-temperature zinc-air battery. *Angew. Chem., Int. Ed.* **2022**, *61*, e202115219.

[27] Han, A. L.; Wang, X. J.; Tang, K.; Zhang, Z. D.; Ye, C. L.; Kong, K. J.; Hu, H. B.; Zheng, L. R.; Jiang, P.; Zhao, C. X. et al. An adjacent atomic platinum site enables single-atom iron with high oxygen reduction reaction performance. *Angew. Chem., Int. Ed.* **2021**, *60*, 19262–19271.

[28] Xu, G. Y.; Nie, P.; Dou, H.; Ding, B.; Li, L. Y.; Zhang, X. G. Exploring metal–organic frameworks for energy storage in batteries and supercapacitors. *Mater. Today* **2017**, *20*, 191–209.

[29] Jiang, Q.; Xiong, P. X.; Liu, J. J.; Xie, Z.; Wang, Q. C.; Yang, X. Q.; Hu, E. Y.; Cao, Y.; Sun, J.; Xu, Y. H. et al. A redox-active 2D metal–organic framework for efficient lithium storage with extraordinary high capacity. *Angew. Chem., Int. Ed.* **2020**, *59*, 5273–5277.

[30] Wu, Z. Z.; Adekoya, D.; Huang, X.; Kiefel, M. J.; Xie, J.; Xu, W.; Zhang, Q. C.; Zhu, D. B.; Zhang, S. Q. Highly conductive two-dimensional metal–organic frameworks for resilient lithium storage with superb rate capability. *ACS Nano* **2020**, *14*, 12016–12026.

[31] Liang, J.; Zhu, G. Y.; Zhang, Y. Z.; Liang, H. F.; Huang, W. Conversion of hydroxide into carbon-coated phosphide using plasma for sodium-ion batteries. *Nano Res.* **2022**, *15*, 2023–2029.

[32] Li, R. Z.; Wang, D. S. Understanding the structure-performance relationship of active sites at atomic scale. *Nano Res.* **2022**, *15*, 6888–6923.

[33] Liu, Z. H.; Du, Y.; Zhang, P. F.; Zhuang, Z. C.; Wang, D. S. Bringing catalytic order out of chaos with nitrogen-doped ordered mesoporous carbon. *Matter* **2021**, *4*, 3161–3194.

[34] Zhao, C. W.; Xu, Y.; Xiao, F.; Ma, J.; Zou, Y. B.; Tang, W. J. Perfluorooctane sulfonate removal by metal–organic frameworks (MOFs): Insights into the effect and mechanism of metal nodes and organic ligands. *Chem. Eng. J.* **2021**, *406*, 126852.

[35] Guo, J.; Yin, Z. H.; Zang, X. X.; Dai, Z. Y.; Zhang, Y. Z.; Huang, W.; Dong, X. C. Facile one-pot synthesis of $NiCo_2O_4$ hollow spheres with controllable number of shells for high-performance supercapacitors. *Nano Res.* **2017**, *10*, 405–414.

[36] Hao, S. Y.; Han, H. C.; Yang, Z. Y.; Chen, M. T.; Jiang, Y. Y.; Lu, G. X.; Dong, L.; Wen, H. L.; Li, H.; Liu, J. R. et al. Recent advancements on photothermal conversion and antibacterial applications over MXenes-based materials. *Nano-Micro Lett.* **2022**, *14*, 178.

[37] Wei, T.; Zhang, M.; Wu, P.; Tang, Y. J.; Li, S. L.; Shen, F. C.; Wang, X. L.; Zhou, X. P.; Lan, Y. Q. POM-based metal–organic framework/reduced graphene oxide nanocomposites with hybrid behavior of battery-supercapacitor for superior lithium storage. *Nano Energy* **2017**, *34*, 205–214.

[38] Fang, R. P.; Chen, K.; Yin, L. C.; Sun, Z. H.; Li, F.; Cheng, H. M. Lithium batteries: The regulating role of carbon nanotubes and graphene in lithium-ion and lithium-sulfur batteries (Adv. Mater. 9/2019). *Adv. Mater.* **2019**, *31*, 1970066.

[39] Jiang, Q.; Lei, Y. J.; Liang, H. F.; Xi, K.; Xia, C.; Alshareef, H. N. Review of MXene electrochemical microsupercapacitors. *Energy Storage Mater.* **2020**, *27*, 78–95.

[40] Ming, F. W.; Liang, H. F.; Huang, G.; Bayhan, Z.; Alshareef, H. N. MXenes for rechargeable batteries beyond the lithium-ion. *Adv. Mater.* **2021**, *33*, 2004039.

[41] Jiang, J. Z.; Bai, S. S.; Zou, J.; Liu, S.; Hsu, J. P.; Li, N.; Zhu, G. Y.; Zhuang, Z. C.; Kang, Q.; Zhang, Y. Z. Improving stability of MXenes. *Nano Res.* **2022**, *15*, 6551–6567.

[42] Zhao, D.; Chen, Z.; Yang, W. J.; Liu, S. J.; Zhang, X.; Yu, Y.; Cheong, W. C.; Zheng, L. R.; Ren, F. Q.; Ying, G. B. et al. MXene (Ti_3C_2) vacancy-confined single-atom catalyst for efficient functionalization of CO_2. *J. Am. Chem. Soc.* **2019**, *141*, 4086–4093.

[43] Zuo, G. C.; Wang, Y. T.; Teo, W. L.; Xie, A. M.; Guo, Y.; Dai, Y. X.; Zhou, W. Q.; Jana, D.; Xian, Q. M.; Dong, W. et al. Ultrathin $ZnIn_2S_4$ nanosheets anchored on $Ti_3C_2T_x$ MXene for photocatalytic H_2 evolution. *Angew. Chem., Int. Ed.* **2020**, *59*, 11287–11292.

[44] Zhang, Y. Z.; El-Demellawi, J. K.; Jiang, Q.; Ge, G.; Liang, H. F.; Lee, K.; Dong, X. C.; Alshareef, H. N. MXene hydrogels: Fundamentals and applications. *Chem. Soc. Rev.* **2020**, *49*, 7229–7251.

[45] Zhang, Y. Z.; Wang, Y.; Jiang, Q.; El-Demellawi, J. K.; Kim, H.; Alshareef, H. N. MXene printing and patterned coating for device applications. *Adv. Mater.* **2020**, *32*, 1908486.

[46] Wu, H.; Almalki, M.; Xu, X. M.; Lei, Y. J.; Ming, F. W.; Mallick, A.; Roddatis, V.; Lopatin, S.; Shekhah, O.; Eddaoudi, M. et al. MXene derived metal–organic frameworks. *J. Am. Chem. Soc.* **2019**, *141*, 20037–20042.

[47] Gund, G. S.; Park, J. H.; Harpalsinh, R.; Kota, M.; Shin, J. H.; Kim, T. I.; Gogotsi, Y.; Park, H. S. MXene/polymer hybrid materials for flexible AC-filtering electrochemical capacitors. *Joule* **2019**, *3*, 164–176.

[48] Wang, X.; Luo, D.; Wang, J. Y.; Sun, Z. H.; Cui, G. L.; Chen, Y. X.; Wang, T.; Zheng, L. R.; Zhao, Y.; Shui, L. L. et al. Strain engineering of a MXene/CNT hierarchical porous hollow microsphere electrocatalyst for a high-efficiency lithium polysulfide conversion process. *Angew. Chem., Int. Ed.* **2021**, *60*, 2371–2378.

[49] Yao, L.; Gu, Q. F.; Yu, X. B. Three-dimensional MOFs@MXene aerogel composite derived MXene threaded hollow carbon confined CoS nanoparticles toward advanced alkali-ion batteries. *ACS Nano* **2021**, *15*, 3228–3240.

[50] Deng, Y. Q.; Shang, T. X.; Wu, Z. T.; Tao, Y.; Luo, C.; Liang, J. C.; Han, D. L.; Lyu, R. Y.; Qi, C.; Lv, W. et al. Fast gelation of $Ti_3C_2T_x$ MXene initiated by metal ions. *Adv. Mater.* **2019**, *31*, 1902432.

[51] Gu, J. W.; Peng, Y.; Zhou, T.; Ma, J.; Pang, H.; Yamauchi. Y. Porphyrin-based framework materials for energy conversion. *Nano Res Energy* **2022**, *1*, e9120009.

[52] Slot, T. K.; Natu, V.; Ramos-Fernandez, E. V.; Sepúlveda-Escribano, A.; Barsoum, M.; Rothenberg, G.; Shiju, N. R. Enhancing catalytic epoxide ring-opening selectivity using surface-modified $Ti_3C_2T_x$ MXenes. *2D Mater.* **2021**, *8*, 035003.

[53] Gan, Q. M.; He, H. N.; Zhao, K. M.; He, Z.; Liu, S. Q. Morphology-

dependent electrochemical performance of Ni-1,3,5-benzenetricarboxylate metal–organic frameworks as an anode material for Li-ion batteries. *J. Colloid Interface Sci.* **2018**, *530*, 127–136.

[54] Armand, M.; Grugeon, S.; Vezin, H.; aruelle, S.; Ribière, P.; Poizot, P.; Tarascon, J. M. Conjugated dicarboxylate anodes for Li-ion batteries. *Nat. Mater.* **2009**, *8*, 120–125.

[55] Yin, X. J.; Chen, X. D.; Sun, W. W.; Lv, L. P.; Wang, Y. Revealing the effect of cobalt-doping on Ni/Mn-based coordination polymers towards boosted Li-storage performances. *Energy Storage Mater.* **2020**, *25*, 846–857.

[56] Jin, J.; Zheng, Y.; Huang, S. Z.; Sun, P. P.; Srikanth, N.; Kong, L. B.; Yan, Q. Y.; Zhou, K. Directly anchoring 2D NiCo metal–organic frameworks on few-layer black phosphorus for advanced lithium-ion batteries. *J. Mater. Chem. A* **2019**, *7*, 783–790.

[57] Lin, X. M.; Niu, J. L.; Lin, J.; Wei, L. M.; Hu, L.; Zhang, G.; Cai, Y. P. Lithium-ion-battery anode materials with improved capacity from a metal–organic framework. *Inorg. Chem.* **2016**, *55*, 8244–8247.

[58] Dong, C. F.; Xu, L. Q. Cobalt-and cadmium-based metal–organic frameworks as high-performance anodes for sodium-ion batteries and lithium-ion batteries. *ACS Appl. Mater. Interfaces* **2017**, *9*, 7160–7168.

[59] Gong, T.; Lou, X. B.; Gao, E. Q.; Hu, B. W. Pillared-layer metal–organic frameworks for improved lithium-ion storage performance. *ACS Appl. Mater. Interfaces* **2017**, *9*, 21839–21847.

[60] Bai, L. Y.; Tu, B. B.; Qi, Y.; Gao, Q.; Liu, D.; Liu, Z. Z.; Zhao, L. Z.; Li, Q. W.; Zhao, Y. L. Enhanced performance in gas adsorption and Li ion batteries by docking Li^+ in a crown ether-based metal–organic framework. *Chem. Commun.* **2016**, *52*, 3003–3006.

[61] Ge, D. H.; Peng, J.; Qu, G. L.; Geng, H. B.; Deng, Y. Y.; Wu, J. J.; Cao, X. Q.; Zheng, J. W.; Gu, H. W. Nanostructured Co(II)-based MOFs as promising anodes for advanced lithium storage. *New J. Chem.* **2016**, *40*, 9238–9244.

[62] Senthil Kumar, R.; Nithya, C.; Gopukumar, S.; Anbu Kulandainathan, M. Diamondoid-structured Cu-dicarboxylate-based metal–organic frameworks as high-capacity anodes for lithium-ion storage. *Energy Technol.* **2014**, *2*, 921–927.

[63] Maiti, S.; Pramanik, A.; Manju, U.; Mahanty, S. Cu_3(1,3,5-benzenetricarboxylate)$_2$ metal–organic framework: A promising anode material for lithium-ion battery. *Micropor. Mesopor. Mater.* **2016**, *226*, 353–359.

[64] Maiti, S.; Pramanik, A.; Manju, U.; Mahanty, S. Reversible lithium storage in manganese 1,3,5-benzenetricarboxylate metal–organic framework with high capacity and rate performance. *ACS Appl. Mater. Interfaces* **2015**, *7*, 16357–16363.

[65] Wu, N.; Yang, Y. J.; Jia, T.; Li, T. H.; Li, F.; Wang, Z. Sodium-tin metal–organic framework anode material with advanced lithium storage properties for lithium-ion batteries. *J. Mater. Sci.* **2020**, *55*, 6030–6036.

[66] Lu, P.; Sun, Y.; Xiang, H. F.; Liang, X.; Yu, Y. 3D amorphous carbon with controlled porous and disordered structures as a high-rate anode material for sodium-ion batteries. *Adv. Energy Mater.* **2018**, *8*, 1702434.

[67] Chen, M. H.; Chao, D. L.; Liu, J. L.; Yan, J. X.; Zhang, B. W.; Huang, Y. Z.; Lin, J. Y.; Shen, Z. X. Rapid pseudocapacitive sodium-ion response induced by 2D ultrathin tin monoxide nanoarrays. *Adv. Funct. Mater.* **2017**, *27*, 1606232.